

Large, Temperature-Tunable Low-Field Magnetoresistance in $\text{La}_{0.7}\text{Sr}_{0.3}\text{MnO}_3:\text{NiO}$ Nanocomposite Films Modulated by Microstructures

Xingkun Ning, Zhanjie Wang,* and Zhidong Zhang

Magnetic properties and low-field magnetoresistance (LFMR) in $\text{La}_{0.7}\text{Sr}_{0.3}\text{MnO}_3$ (LSMO):NiO nanocomposite films grown on SrTiO_3 (001) substrates have been investigated, which are shown to be tunable with different microstructures. The LSMO:NiO nanocomposite films with NiO volume ratio of 50% have a checkerboard-like structure and show a large LFMR in a temperature range from 200 to 300 K ($\approx 17\%$ at 250 K with a magnetic field of 1 T). As the NiO volume ratio is increased to 70%, a nanocolumnar structure formed in the films. Their LFMR is significantly enhanced at a wide temperature range of 10–210 K. The highest value of LFMR with 41% was achieved at 10 K in a magnetic field of 1 T. The enhanced LFMR can be considered to result from the electron scattering at the ferromagnetic LSMO/NiO interfaces and magnetic tunnel junctions (MTJs) of LSMO/NiO/LSMO at the nanometer scale. Our results demonstrate that large and tunable LFMR from low temperature to room temperature can be realized by controlling the microstructures in the epitaxial $\text{La}_{0.7}\text{Sr}_{0.3}\text{MnO}_3:\text{NiO}$ nanocomposite thin films, which will be expected to be applied in the devices using for a wide temperature range.

1. Introduction

Lanthanum manganite perovskites $\text{La}_{1-x}\text{A}_x\text{MnO}_3$ (A is a divalent cation) with a Curie temperature (T_C) above room temperature, such as $\text{La}_{0.7}\text{Sr}_{0.3}\text{MnO}_3$ (LSMO) have attracted great attention due to their complex magnetic properties and the giant magnetoresistance (GMR) occurring around the T_C .^[1–3] These GMR materials are particularly interesting as designing the memory-readers of digital device, magnetic sensor, p - n junctions or spintronic applications involving GMR effect with the high- T_C superconductivity.^[4–7] However, the intrinsic GMR value in this system can only be triggered at a high magnetic field of several Teslas and within a narrow temperature range,^[8] which obstructed applications such as magnetic head sensors or low-cost magnetic sensors that should be operated at a low magnetic field and stable temperature-sensitive

environment.^[9,10] Recently, due to the deepening cognition of the intrinsic and extrinsic GMR effect, growing attention has been paid to polycrystalline manganites to obtain the extrinsic low-field magnetoresistance (LFMR) by structuring grain boundaries, nanosized inclusions, interface phase, and artificial grain boundaries. What's more, the LFMR in composites or films can be further improved by introducing a secondary phase (usually non-magnetic or antiferromagnetic insulators).^[11–20] For example, the LFMR values of -6% at 5 K and 0.16 T in LSMO: SrTiO_3 superlattice structure,^[3] -17.5% at 30 K and 1 T in LSMO: ZnO columnar structure,^[21] -8% at 10–150 K and 1 T in LSMO: MgO nanorod arrays structure^[22] and -12% at 77 K and 0.4 T in LSMO:Ag 0–3 structure^[23] have been reported. However, neither the early results obtained from LSMO polycrystalline films^[24] or recent results obtained from LSMO: ZnO

composite films with a columnar structure,^[21] enhanced LFMR values are always display in a low temperature range. That may be due to the large grain size in polycrystalline films ($\approx \mu\text{m}$) or weak spin coupling at the phase boundaries in the composite thin films. Systems featuring a large LFMR at temperatures close to or even higher than room temperature are also interesting owing to their potential applications in magnetic field sensing and data storage.^[25] Dey et al. have found that the large LFMR will keep steady in a higher temperature range when the grain size is in nanoscale and gets pronounced with the decrease in particle size.^[26] It is notable that the spin pinned effect occurs at the nanosized grain surface defect sites or spin coupling at the boundaries.^[26,27] In addition, the short range ferromagnetic (FM) coupling order may add the opportunity of spin scattering even near the Curie temperature.^[28,29] Thus it is speculated that the high-temperature LFMR in LSMO composite films can be got through tuning the grain size and the FM coupling at the phase boundary. MacManus-Driscoll et al. proposed that the self-assembled composite films are free from substrate clamping constraints and form strained vertical interface areas which can be used to tune the FM coupling by another phase and also can provide a more flexible way to control the growth of the films which can be used to control the grain size to get enhanced physical properties.^[30] To prepare the LSMO-based composite films, on the one hand, it should

X. K. Ning, Prof. Z. J. Wang, Prof. Z. D. Zhang
Shenyang National Laboratory for Materials Science
Institute of Metal Research (IMR)
Chinese Academy of Sciences (CAS)
72 Wenhua Road, Shenyang 110016, China
E-mail: wangzj@imr.ac.cn



DOI: 10.1002/adfm.201400735

be noted that the addition of second metallic oxide (MO) phase, such as ZnO,^[31–34] V₂O₃^[20] and Mn₃O₄^[1] etc., may induced self-assemble columnar growth due to a large lattice mismatch with the matrix.^[30,35,36] However, one major challenge for enhancing the LFMR in a high temperature range in the composite films is how to tune the crystalline grain size of the second MO phase. It is also noted that in the LSMO composite thin films, if LSMO phase contacts with an insulator phase and then other LSMO phase forming a LSMO/insulator/LSMO structure, a magnetic tunneling junction (MTJ) can be formed. The MTJs of LSMO/insulator/LSMO are important to enhance the LFMR properties of composite films. To achieve this object, the major challenge is how to control the grain size of the insulator phase within 1–2 nm, which is the optimized thickness of a middle layer in a MTJ structure.^[37,38] In addition to this, to modulate the geometry distribution of these nano-sized MTJs may favor the artificial designing of the LFMR properties. For the composite films, the small size and large aspect ratio of nano-structure insulator phase would favor the LFMR, because the insulator tunneling barriers and the scattering centers at the phase interface enhance with reducing the grain size of the insulator phase.^[12,26,39] On the other hand, there are few reports on the enhanced LFMR and its temperature by exploiting the second MO phase with interfacial FM or antiferromagnetic (AFM) order due to the spin polarization at the interface and coherence of the tunneling electrons of LSMO.^[40] In our previous study, we investigated the magnetic properties of the LSMO/NiO interface and found that the Ni-O-Mn has FM interaction through the electron transfer.^[41] The interface FM interaction states would add the opportunity of scattering and make the resistivity rise.^[29] In addition, the pinned FM domain rotation effects at the boundaries could induce the magnetoresistance effect in LSMO polycrystalline samples near Curie temperature and therefore decreased the GMR field at a high temperature range.^[8] Hence, the enhanced LFMR in a wide temperature range may be realized by controlling the geometry structures of NiO with LSMO in the LSMO:NiO nanocomposite thin films.

In this paper, typical antiferromagnetic NiO has been used to fabricate LSMO:NiO nanocomposite thin films with different microstructures grown epitaxially on SrTiO₃ (STO) (001) substrates by pulsed laser deposition (PLD). First, the composite thin films with a nano-columnar structure have been deposited by using a method reported by Kang et al.^[34] For fabricating the composite film with different geometry microstructures, we tune the nano-columnar structures by depositing 2D LSMO pure layer and inserting the columnar structure with 1–2 nm in thickness. So a nano-chessboard-like structure^[42] along the out-of plane direction has been created in our experiments. Then the nano-columnar and nano-chessboard-like structures in one system have been successfully prepared. For comparison, LSMO:NiO composite films with a multilayer structure were also prepared. Detail information of the growth modes have been discussed in the supplementary materials (Supporting information, Figure S1 and Figure S2). The composite thin films with the nano-columnar structure show an enhanced LFMR in a low temperature range, while the composite thin films with the checkerboard-like structure show an enhanced LFMR in a high temperature range, which may be suitable for the application in room temperature devices.

2. Results and Discussion

The NiO ratios in these samples have been determined by the energy dispersive x-ray spectrometer (EDS) in the cross-section and x-ray photoelectron spectroscopy (XPS). The nanocomposite thin films with various volume ratios of LSMO and NiO will hereafter be denoted as (LSMO)_{10-x}:(NiO)_x (10:x), where x represents NiO ratio. The (LSMO)_{1-x}:(NiO)_x (x<6) shows the nano-checkerboard-like structure growth mode while when x>6, the composite thin films shows nano-columnar structure growth mode. As the typical samples, we will discuss the (LSMO)₅:(NiO)₅ and (LSMO)₃:(NiO)₇ thin films in detail.

The XRD patterns for the pure LSMO film, (LSMO)₅:(NiO)₅, (LSMO)₄:(NiO)₆ and (LSMO)₃:(NiO)₇ composite films on the STO (001) substrate are shown in Figure 1a. The pure LSMO film exhibits a highly (00l)-textured orientation. For the composite films, there is a prominent peak for NiO (200) compared with the pure LSMO film and no other peaks of NiO are detected. The LSMO in the composite films also exhibits a highly (00l)-textured orientation. However, compared with the pure LSMO film, the position of the LSMO (002) peak in the composite films shifted to the left side of the STO (002) peak, as shown in Figure 1b of the enlarged LSMO(002) region. The

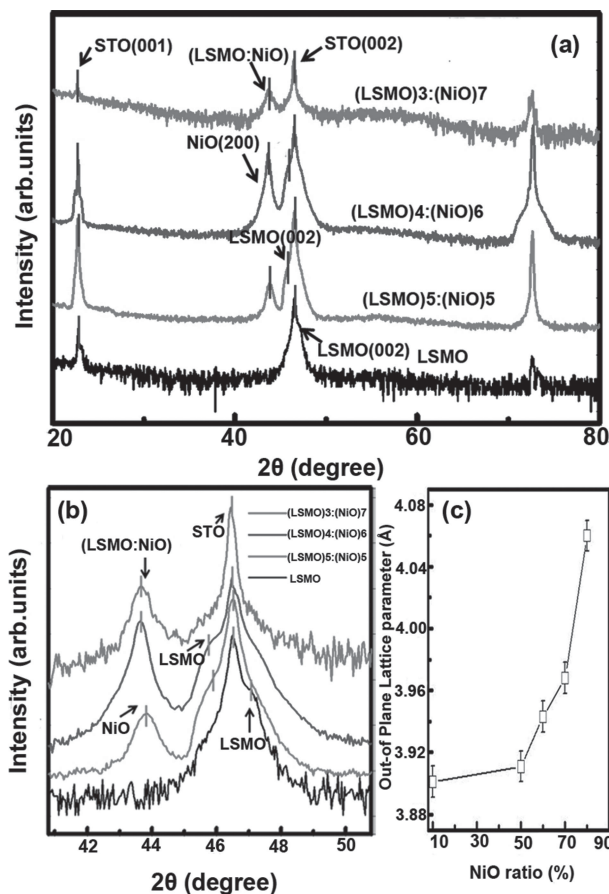


Figure 1. a) XRD patterns of the LSMO film, (LSMO)₅:(NiO)₅, (LSMO)₄:(NiO)₆ and (LSMO)₃:(NiO)₇ composite films and b) an enlarged XRD scan around the STO(002) peak. c) d-spacing of out-of plane of LSMO phase versus NiO ratio.

corresponding d spacing of the out-of plane for the LSMO phase is determined to be 3.943 Å and 3.968 Å for the $(\text{LSMO})_5:(\text{NiO})_5$ and $(\text{LSMO})_4:(\text{NiO})_6$, respectively, which are larger than that (3.901 Å) in the pure LSMO films. This is possibly due to the lattice mismatch between LSMO and NiO (about 6%). In the $(\text{LSMO})_3:(\text{NiO})_7$ composite films, the LSMO (002) peak further left-shifted and overlaps with the NiO (200) peak (Figure 1b), implying that the strain in the films becomes large with increasing NiO ratio. Figure 1c shows the out-of plane lattice parameter as a function of NiO concentration. The lattice parameter increases rapidly with high NiO ratio (60–70%), but is almost constant at low NiO concentration (0–50%). All the composite films show that the LSMO phase is in a tensile stress state along out-of plane direction, which can be tuned by the NiO phase. The following TEM study results will show that the composite films with 50% NiO ratio have a nano-checkerboard-like structure (Figure 2), while the composite films with 70% NiO ratio have a nano-columnar structure (Figure 3). Therefore, the vertical strain of LSMO is much larger in the nano-columnar structure than that in the nano-checkerboard-like structure. The vertical interface strain dominates in the composite films with the nano-columnar structure which is in conformity with the results in the LSMO:ZnO vertically aligned composite thin films.^[30,43] However, the in-plane and out-of plane lattice of the LSMO phase coherently match in the columnar part and the planar pure LSMO part across the nano-checkerboard-like structure, which is energetically favorable for the growth because the LSMO phase in different parts is continuous connect. Then the out-of plane lattice parameter of the LSMO phase did not increase so much as that in the nano-columnar structures. Under this circumstance, the out-of plane lattice parameter of the NiO phase will decrease to match with the LSMO phase, so that the position of the NiO (200) peak in the composite films right-shifted, as shown in Figure 1b. In the following, the transmission electron microscopy (TEM) study results will further indicate that LSMO and NiO columnar grains are epitaxially grown on the STO substrate and have clear and sharp interfaces with each other. Therefore, the out-of-plane lattice of the LSMO phase expanded for matching with that of the NiO phase. The large strain due to the lattice matching will decrease T_C of the LSMO phase, because the double exchange interaction is weakened due to the strain-induced modification in the Mn-O-Mn bond length and angle.^[44]

To further characterize the microstructures and the epitaxial nature of the composite films, TEM study has been conducted. Figure 2a and Figure 3a show low-magnification TEM images for the $(\text{LSMO})_5:(\text{NiO})_5$ and $(\text{LSMO})_3:(\text{NiO})_7$ films with a thickness of 44 and 45 nm, respectively. It can be seen that the interface between the film and substrate in the samples is sharp and flat (indicated by the red dashed arrows). Figure 2b shows a high-resolution TEM (HRTEM) image of the $(\text{LSMO})_5:(\text{NiO})_5$ composite films. It is clearly exhibited that NiO and LSMO are two-phase separation forming a checkerboard-like structure along the out-of plane direction (also can be seen from Figure S3 and Figure S4, Supporting Information). The grains of the NiO phase are 1–2 nm in size, and the width of the LSMO between the NiO phases is about 1 nm. The d -spacing of the out-of plane of the LSMO phase is determined to be 3.94 Å, as shown in Figure 2c–2e, corresponding with the XRD result.

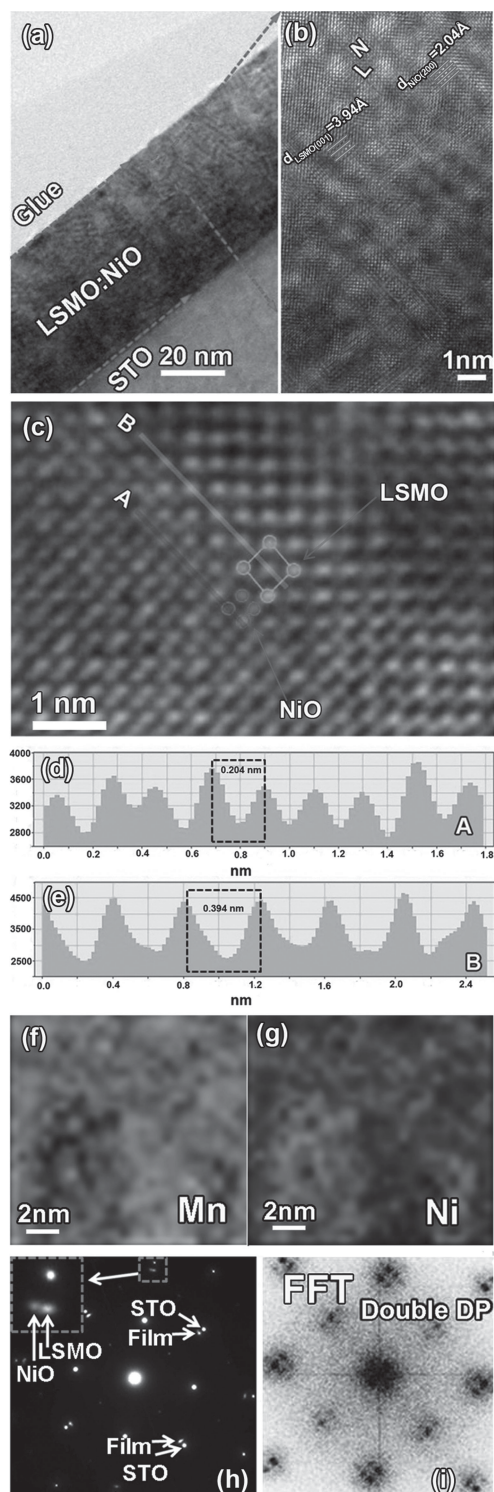


Figure 2. a) A cross-sectional TEM image of the $(\text{LSMO})_5:(\text{NiO})_5$ composite film with 44 nm thickness, b) A HRTEM image of the $(\text{LSMO})_5:(\text{NiO})_5$ composite film. “L” stands for LSMO phase and “N” stands for NiO phase. c) A HRTEM image of the LSMO/NiO interface, and d–e) its corresponding intensity line profiles of two neighboring NiO and LSMO (indicated by A and B in the HRTEM images). f–g) EDS mapping of Mn (orange) and Ni (red) elements in the sample. h) SEAD patterns and i) the Fast Fourier Transformation (FFT) patterns transformed from the HRTEM image of (b).

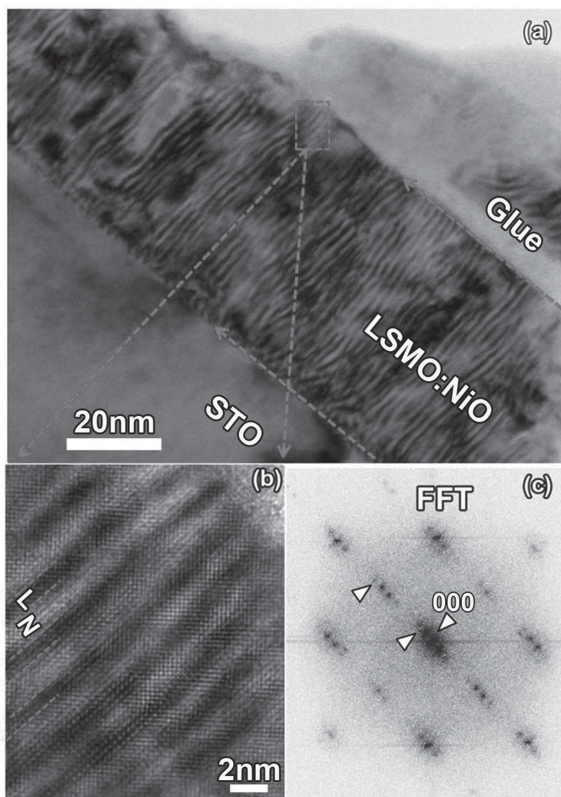


Figure 3. a) A Cross-sectional TEM image of the $(\text{LSMO})_3:(\text{NiO})_7$ composite film with 45 nm thickness. b) An HRTEM image of the composite films. “L” stands for LSMO phase and “N” stands for NiO phase. Insert: the Fast Fourier Transformation (FFT) patterns transformed from the HRTEM image of (b).

Figures 2 and 2g show the typical EDS mapping of Mn (orange) and Ni (red) elements in the sample. Given the resolution of the TEM instruments (F20, Tecnai), it is difficult to figure out the squared grain of the LSMO and NiO in such a small size. However, the nano-sized NiO and LSMO phases were separated with each other according to the EDS mapping. This is due to the fact that the radius of Ni^{2+} ions (0.69 Å) is larger than that of Mn^{3+} or Mn^{4+} (0.58 Å and 0.53 Å, respectively), and the larger ion difficultly enters into the lattice and probably is being pushed out towards the grain boundary in order to release the local strain.^[45,46] Additionally, the selected-area electron diffraction pattern (SAED) is given at the same orientation with the HRTEM image, both taken along the [001] zone axis of the STO substrates, as shown in Figure 2h. The distinct diffraction dots from LSMO and NiO in the enlarged SAED image also confirm that LSMO and NiO separate in the checkerboard-like structure. From the Fast Fourier Transformation (FFT) patterns (Figure 2i) transformed from the HRTEM image, the second order reflection of the (100) and (001) planes can be clearly observed. Double-diffraction spots are visible around each of these primary reflections. They also surround the direct beam, although it is hidden by the flare from that beam. The double diffraction is a common feature for two-phase materials exhibiting epitaxy or topotaxy properties.^[47] The analytical results obtained in this study are also in line with those of the

checkerboard microstructures in $(\text{Nd}_{7/12}\text{Li}_{1/4})\text{TiO}_3$ reported by Guiton et al. and in decomposing deposited films reported by Ni et al.^[48,49] By contrast, a nano-columnar structure could be obtained in the $(\text{LSMO})_3:(\text{NiO})_7$ films. Figure 3a shows a cross-sectional TEM image of the $(\text{LSMO})_3:(\text{NiO})_7$ films. It can be clearly seen that the nano-column from the bottom to top filled the entire film. Figure 3b shows a cross-sectional HRTEM image for the films. The red broken lines indicate the interfaces between the LSMO and NiO phases. It is clear that columnar grains of the LSMO and NiO phases are epitaxially grown on the STO substrate and have clear and sharp interfaces between each other. The HRTEM images also indicate that a well-ordered superlattice structure along the in-plane directions has been formed in the $(\text{LSMO})_3:(\text{NiO})_7$ films. Furthermore, the crystal orientation relationships between the film and substrate are revealed as $(001)_{\text{LSMO}}// (001)_{\text{STO}}$ and $(002)_{\text{NiO}}// (001)_{\text{STO}}$, and between LSMO and NiO are determined to be $(001)_{\text{LSMO}}// (002)_{\text{NiO}}$ with a lattice mismatch of 6%. A large expansion of the d spacing in the out-of plane direction has been found in LSMO phase, where the lattice parameter is determined to be 4.06 Å matching with the NiO (100) planes, which is consistent with the XRD data. Figure 3c is the corresponding FFT patterns transferred from Figure 3b. Interestingly, the regular superlattice spots also reveal that a superlattice structure^[47,50] appears along the in-plane direction which is perpendicular to the growth direction. The results have been indicated by XRD data (Figure 1c). The average grain size of the NiO phase is 1–2 nm in diameter. Based on the TEM results above, typical depictions for the checkerboard-like structure and the nano-columnar structure are illustrated in **Figure 4**. The green part represents the LSMO phase, while the red part represents the NiO phase. In the $(\text{LSMO})_5:(\text{NiO})_5$ composite films, the LSMO/NiO/LSMO (L/N/L) structures are separated by the ultra-thin LSMO planar layers. In the $(\text{LSMO})_3:(\text{NiO})_7$ composite films, the columnar L/N/L structures along the in-plane directions connect with each other. In both composite films, the NiO phase with 1–2 nm thicknesses in L/N/L structures forms the MTJ structures, where NiO as a semiconductor tunneling layer which is correspondence to the LSMO/insulator/LSMO (FM/I/FM) structure.^[51,52] Therefore, the L/N/L exactly constitutes a MTJ-like structure. The L/N/L structures and their geometrical arrangement in these composite films will affect the LFM properties of the films, and we will discuss their effect in the following.

Figure 5a presents the temperature dependence of field cooled (FC) magnetization of the films with different NiO ratios with an in-plane magnetic field $H = 0.01$ T. For all the films, the magnetization decreases with increasing temperature, and the

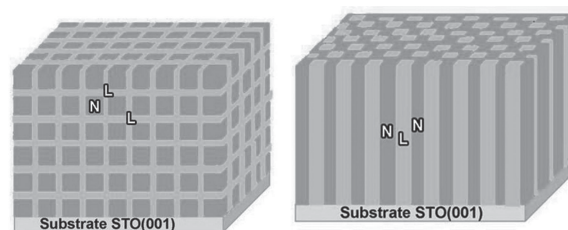


Figure 4. Schematic illustrations of a) the ideal checkerboard-like structure and b) the nano-columnar structure in the nanocomposite thin films.

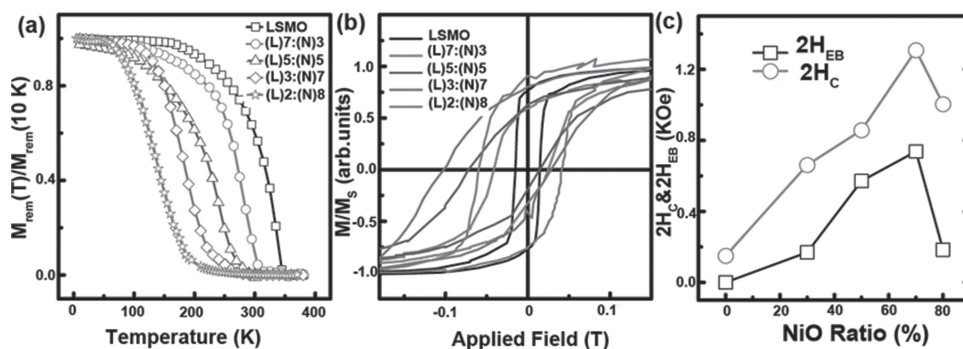


Figure 5. a) Temperature dependence of field cooling (FC) magnetization normalized by their value at 10 K. b) Magnetic hysteresis loops of $(\text{LSMO})_{1-x}:(\text{NiO})_x$ composite thin films at 10 K along in-plane direction. “L” stands for LSMO phase and “N” stands for NiO phase. Magnetization is normalized by the saturated value. c) Exchange bias field H_{EB} and coercivity H_C versus NiO ratio.

transition from FM to paramagnetic (FM-to-PM) is observed. The transition temperature T_C is determined to be 340 K for the pure LSMO film, which is in line with recent experimental reports.^[41] In addition, T_C shifts to a lower temperature with increasing NiO ratio (Figure S5, Supporting Information). The strain in the films increases with increasing NiO ratio, as described from the XRD and HRTEM results, resulting in the decrease of the electron transfer integral of the $\text{Mn}^{3+}\text{-O-Mn}^{4+}$, because of the change in the length and angle of Mn-O-Mn bonds.^[53] It should be noted that the decrease of T_C can be explained by other reasons, such as the small radial grain size or the ultra-thin thickness of the shell-LSMO, Ni-O-Mn magnetic interaction at the interface.^[54,55] Moreover, the NiO nanoparticles increase the magnetically disordered states and change the Mn-O-Mn bond length and angle, and therefore the exchange energy decreases. The magnetic hysteresis loops normalized by the maximal magnetization at 5 K, recorded after field cooling (FC) at 0.4 T from 340 K down to the measurement temperature, are shown in Figure 5b. It is clearly seen that hysteresis loops shifted along the magnetic-field axis, indicating the existence of the exchange bias effect. When switching the field both in FC process and in hysteresis loops measurement from in-plane to out-of-plane, we also obtain a similar magnitude of exchange bias field. The absolute value of the EB field is about 380 Oe for the (LSMO)3:(NiO)7 samples and is larger than those in the LSMO/SrTiO₃ superlattice and LSMO/BiFeO₃ bilayer.^[3,56] The EB field is also much larger than those in the LSMO/NiO bilayer obtained in our previous study ($H_{EB} = 60$ Oe^[41]) and LSMO/NiO multi-layered structure ($H_{EB} = 105$ Oe, in this study). The large EB field can be considered to be due to the enhanced interfacial areas in the nanocomposite films as described by Choi et al. in the self-assembled BiFeO₃-Fe₃O₄ nanocomposite heteroepitaxial films.^[57] Recently, Choi et al. have shown that in self-assembled, nanocomposite heteroepitaxial films of BiFeO₃ containing embedded Fe₃O₄ nanoplates, a high exchange bias value of 40 Oe was achieved at room temperature.^[57] The exchange bias field H_{EB} and coercivity H_C , interestingly, first increase and then decrease with increasing the NiO ratio, as shown in Figure 5c. Actually, on the basis of the microstructure model in Figure 4a, the ratio of the pinned interface area increase from zero to a maximum value with the NiO addition. However, as the NiO ratio increases from 70% to 100%, the effective pinned interface area

decrease rapidly to zero. Since the exchange bias is an interfacial effect by the ferromagnetic interaction between LSMO and NiO, and the exchange bias field H_{EB} and coercivity H_C increase with increasing the pinned interface ratio. In addition to this, one may anticipate that the large aspect ratio of the artificial interface would enhance the efficiency of the NiO barriers which can be described as phase boundary energy as discussed below and thus enhance the LFMR effect. Moreover, the pinned neighboring LSMO domains add the interface scattering effect will affect the LFMR near the room temperature as reported in double perovskite La₂NiMnO₆.^[58] Figure 6 shows the FM interface state at the extra fields. By analogy, the random uncompensated spins pinned at the interface exist and thus enhanced the coercivity. The short range ordering at the interface at a low field ($H < H_C$) will add the opportunity of spin scattering and makes the LFMR enhanced.^[28] It should be noted that the short range FM gradually disappears as the extra field increases ($H > H_C$). The resistance decreased due to the alignment of the intergrain spins and thus the LFMR increased. The LFMR results of the (LSMO)5:(NiO)5 films with the checkerboard-like structure and the (LSMO)3:(NiO)7 films with the nano-columnar structure will be studied below in detail.

Figure 7a shows the temperature dependence of resistivity $\rho(T)$ for the (LSMO)5:(NiO)5 and (LSMO)7:(NiO)3 composite films and the pure LSMO film in different magnetic fields. It can be seen that the pure LSMO film displays an insulating-metallic (IM) transition temperature ($T_{IM} = 340$ K, see the inset

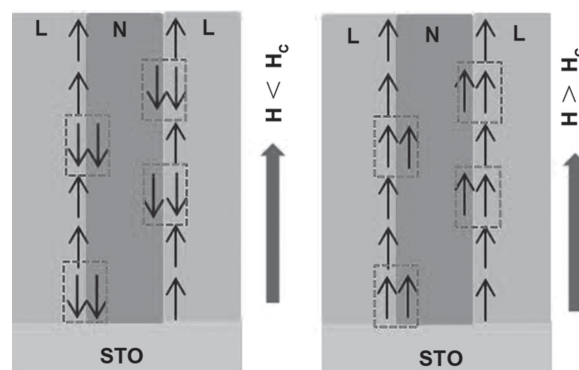


Figure 6. Schematic illustrations of FM interaction at the LSMO/NiO interfaces in a low field and a high field.

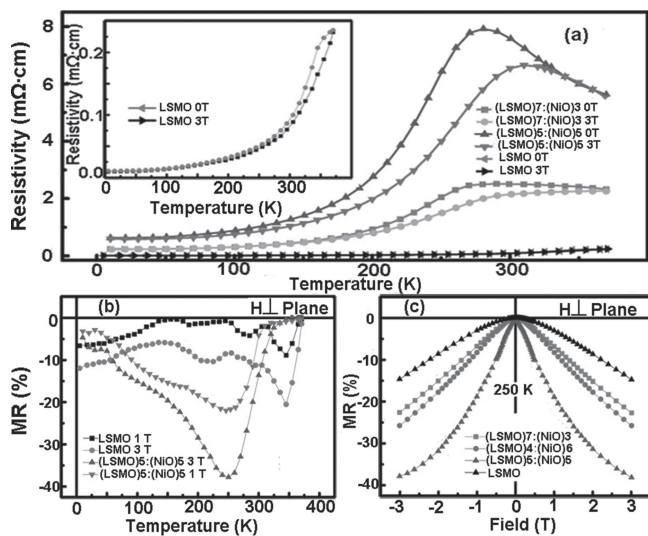


Figure 7. a) Temperature dependence of the resistivity at 0 T and 3 T for the (LSMO)₃:(NiO)₇ and (LSMO)₅:(NiO)₅ composite films, and the pure LSMO films. b) Absolute MR values with 1 T and 3 T for the (LSMO)₅:(NiO)₅ composite films and the LSMO pure film. c) Magnetic field dependent MR% for the (LSMO)₇:(NiO)₃, (LSMO)₅:(NiO)₅ and (LSMO)₃:(NiO)₇ composite films, and the pure LSMO films.

of Figure 7a), which is defined as the temperature at the maximum resistance in $\rho(T)$ data, and is close to T_C in Figure 5a. The T_{IM} of the composite films do not couple to T_C and shift gradually to a lower temperature with increasing NiO concentration. The resistivity of the composite films increased with NiO ratio over the whole measured temperature region. The increase in resistivity as well as down-shift of T_{IM} in the composite films as the addition of the NiO phase may be due to the increase of higher resistive phase boundary, which have been reported by Chen et al.^[21] In order to give support to this statement, the relative phase boundary energy has been estimated by using the adiabatic small-polaron hopping model: $\rho = \rho_0 T \times \exp(E/k_B T)$ reported by Teresa et al.,^[17,59] where E can be suggest as the height of the phase boundary energy. The value of E increases with increasing NiO concentration in the composite films (insert of Figure S7a, Supporting Information). In Figure 7b, under the out-of-plane applied field of 3 T, there is obvious magnetoresistance in the (LSMO)₅:(NiO)₅ composite films around near-room temperature as compared with the pure LSMO film. The MR data, as shown in Figure 7b, which is defined as $MR\% = \{[\rho(H, T) - \rho(0, T)]/\rho(0, T)\} \times 100\%$, where $\rho(H, T)$ and $\rho(0, T)$ are the temperature dependent resistivity values under applied field (1 T and 3 T) and zero field. The maximum value of about 17% under applied field of 1 T is observed at 250 K in the (LSMO)₅:(NiO)₅ composite film. This strong LFM broad peak locates around the high temperature range (200–300 K). As expected, the magnetic field dependent out-of-plane isothermal MR% of the (LSMO)₅:(NiO)₅ composite film at 250 K after zero-field cooling (ZFC) process increases rapidly with increasing the applied field. The (LSMO)₅:(NiO)₅ composite film shows larger MR values at all measured fields as compared to the pure LSMO and other composite films, as shown in Figure 7c.

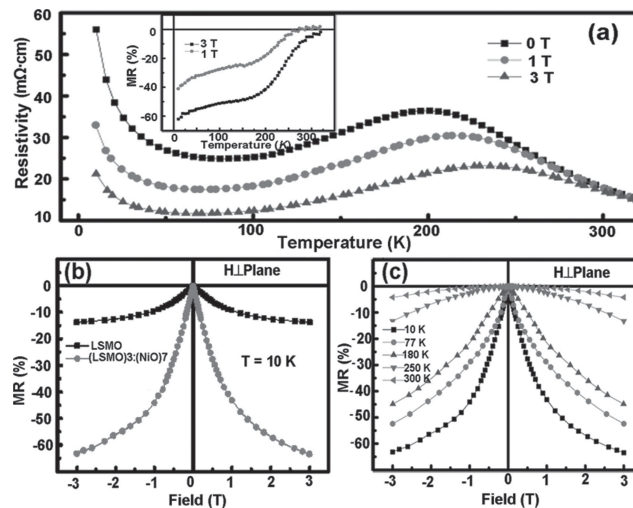


Figure 8. a) Temperature dependence of the resistivity at 0 T, 1 T and 3 T for the (LSMO)₃:(NiO)₇ composite films. Insert: MR% values with 1 T and 3 T versus temperature for the (LSMO)₃:(NiO)₇ composite films. b) Magnetic field dependent MR% for the (LSMO)₃:(NiO)₇ composite films at 10 K. c) Magnetic field dependent MR% for the (LSMO)₃:(NiO)₇ composite films at different temperatures.

Figure 8a shows the temperature dependence of resistivity $\rho(T)$ curves for the (LSMO)₃:(NiO)₇ composite films in an external magnetic field. It is obviously different from the (LSMO)₅:(NiO)₅ composite films and the LSMO pure films. A minimum of resistivity appeared at 80 K, corresponding to the MIT temperature T_{MI} , after which the resistivity shows insulating-like behavior in the entire rest temperature range. Similar phenomena have been reported in the (LSMO)₃:(ZnO)₇, LSMO:CoFe₂O₄, and LSMO:MgO systems.^[32,60,61] This upturn portion of the resistivity has been fitted by using the Coulomb blockade model:^[62] $\rho = \rho_0 \exp(T_0/T)^{1/2}$, where T_0 depends on the tunneling barrier height.^[19] The value of T_0 increases with increasing NiO ratio as the result of the increase of the tunneling barrier height (Figure S7b). It is clear that the high ratio of semiconductor NiO phase can significantly affect the resistivity, because the overall resistivity increases with increasing the NiO concentration and the ground state shows that the NiO has low transport properties at low temperatures. The MR% plots with the temperature for the (LSMO)₃:(NiO)₇ under the out-of-plane external field of 1 T and 3 T are shown in insert of Figure 8a. It should be noted that MR% values of this sample increase gradually as the temperature decreases from room temperature to low temperatures. The maximum value of about 41% under an applied field of 1 T is obtained at 10 K ($\approx 62\%$ at 3 T). In addition, the enhanced LFM across a broaden temperature range from 10 K to 210 K ($\approx 17\%$, 210 K; 1 T) has been observed. The field dependent resistivity values $\rho(H)$ measured at different temperatures have been shown in Figures 8 and 8c. It can be seen that the absolute value of MR% increases with the increase in the magnetic field. A sharper increase of the MR% value at a low field (less than 1 T) has been observed in the composite film compared to the pure LSMO film, as shown in Figure 8b. The increase in MR% value is believed to relate to

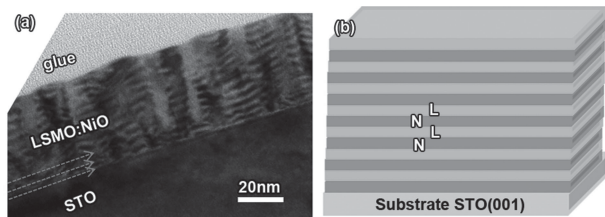


Figure 9. a) A cross-sectional TEM image of the multilayered LSMO:NiO composite film with 41 nm thickness. b) A schematic illustration of the multilayer structure.

the spin-tunneling effect based on the MTJ structure between the interfaces LSMO/NiO. The enhanced LFMR behavior is also found at high temperatures, as shown in Figure 8c, corresponding with the MR% versus temperature data. To further understand the relationship between the magnetoresistance properties and microstructure in the composite films, multilayered LSMO:NiO composite films have also been prepared. **Figure 9a** shows a cross-sectional view of the LSMO:NiO film with a multilayer structure, while **Figure 9b** shows an illustration of the ideal multilayer structure. In this structure, the NiO ratio is about 60% compared with the LSMO matrix. However, the LFMR values of these composite films are very small in the total temperature range. The experimental results above proved that the L/N/L structures and their geometrical arrangement in these composite films are very important for enhancing the LFMR properties. The LFMR value and triggered temperature (17%; 1 T, 250 K) in (LSMO)₅:(NiO)₅ composite films reported here are higher than those previously reported: 15% at 1 T and 170 K^[31] and 17.5% at 1 T and 40 K^[33] for LSMO:ZnO composite films. The LFMR temperature range (MR% ≥ 17%; 2–210 K) in the (LSMO)₃:(NiO)₇ composite films of our experimental results, is broader than those in the LSMO:MgO composite film (MR% ≥ 17%; 10–150 K) reported by Li et al.^[22] and in LSMO:ZnO composite films (MR% ≥ 10%; 10–160 K) reported by Zhang et al.^[32] Our results imply that the LSMO:NiO nanocomposite thin films with a large LFMR in the higher temperature range may be suitable for the application in room-temperature devices, including memory-readers of digital devices or random-access memory.

According to the experimental results above, we assume that the microstructure plays an important role to modulate the magnetoresistance properties of these composite films. Namely, the tunneling resistance of the MTJs of L/N/L can enhance the LFMR. Meanwhile, tuning the spatial distribution of these MTJs by modulating the microstructure in the composite thin films, as depicted in **Figure 4**, can effectively change the conducting networks which determine the total electron transport properties. Ideally, the (LSMO)₅:(NiO)₅ films can be depicted as a series of high resistant MTJs parallel with the low resistant LSMO transport paths, while the (LSMO)₃:(NiO)₇ films can be depicted as numerous MTJs in-line together. In addition, the LSMO:NiO films with multilayer structure can be depicted as a series high resistant NiO barriers and low resistant LSMO transport paths without any MTJs along the in-plane directions. Therefore, a series parallel circuit model can be adopted to explain the MR effect which has been applied to explain the transport properties.^[63] Fedoseev et al. have proposed the

dimensional RC network model based on the microstructures of the films to phenomenologically describe the transport properties of the La_{2/3}Ca_{1/3}MnO:STO composite films.^[14] In this study, we will use the series parallel circuit model to understand the transport properties in the checkerboard-like (LSMO)₅:(NiO)₅ composite films, nano-columnar (LSMO)₃:(NiO)₇ composite films and the multilayered LSMO:NiO films. **Figures 10** (a–c) show the schematic diagrams for the electric circuits in these cases, respectively. The green part represents the LSMO phase with a low resistivity, while the red part represents the NiO phase with a high resistivity. The green-red-green sets stand for the MTJ of LSMO/NiO/LSMO. The NiO tunneling effect and the Ni-O-Mn FM interaction can be triggered in a small field, and therefore will enhance the LFMR. Firstly, for the composite film with the checkerboard-like structure, electric current can flow through two kinds of channels: the LSMO phase and the MTJs of LSMO/NiO/LSMO (**Figure 10a**). The overall resistivity in the whole temperature range can be described by $1/\rho = A(H)/\rho_{\text{LSMO}} + B(H)/(\rho_{\text{MTJ}} + \rho_i)$, where ρ_{LSMO} , ρ_{MTJ} and ρ_i denote the resistivity for the LSMO phase, the MTJs of LSMO/NiO/LSMO and the additional resistance derived from the LSMO/NiO interface, respectively. $A(H)$ and $B(H)$ are the weight factors depending on the magnetic field. In composite films with low NiO concentrations, such as (LSMO)₇:(NiO)₃ and (LSMO)₆:(NiO)₄, the LSMO space layer is thick and the resistance $\rho_{\text{LSMO}} \ll \rho_{\text{MTJ}}$ and ρ_i . In this case, the transport properties mainly depends on the ρ_{LSMO} and the factor $A(H)$. As the thickness of the LSMO space layer decreases, the ρ_{LSMO} increases due to the interface scattering effect until $\rho_{\text{LSMO}} \approx \rho_{\text{MTJ}}$. Therefore, with increasing NiO concentration to 50% in this structure, the total resistivity is increased not too much, compared with the nano-columnar structure due to the LSMO transport channel. However, in the low temperature range, the resistivity of the LSMO is much lower than that of the ρ_{MTJ} and the factor $B(H)$ can be largely tuned by the magnetic field due to the spin-polarized tunneling effect through the local LSMO/NiO/LSMO junctions. In addition, the rotation of the pinned micro-neighboring LSMO domains in a low field together with the interface scattering effect of the LSMO/NiO interface can also enhance the LFMR in high temperatures.^[8,58] In a low temperature range, the total resistivity depends on the ρ_{LSMO} transport channels and shows weak LFMR properties. Therefore the composite films with checkerboard-like structure have

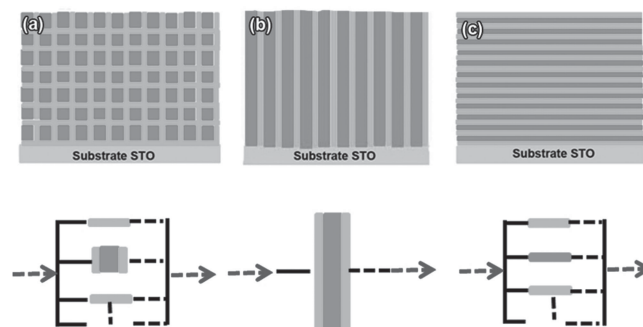


Figure 10. Schematic illustrations of a simple circuit model for a) the checkerboard-like structure, b) the nano-columnar structure and c) the multilayer structure.

the enhanced LFMR in the high temperature range. Secondly, for the composite film with the nano-columnar structure, electric current flows through only one kind of channel of the MTJs of L/N/L (Figure 10b). Therefore, its overall resistivity can be given by $\rho = A'(H)\rho_{\text{LSMO}} + B'(H)\rho_{\text{MTJ}} + C(H)\rho_{\text{i}}$, where $A'(H)$, $B'(H)$ and $C(H)$ are the weight factors depending on the magnetic field. The large resistivity of this film is determined by the high resistance of the MTJs (L/N/L) and the phase boundary of LSMO/NiO throughout the whole temperature range. Especially, in the low temperature range, the ground state is basically determined by the AFM semiconductor NiO. It also should be noted that $B'(H)$ which represents the LFMR effect can be tuned via the scattering effect in the FM-LSMO/NiO interface by the applied field. Therefore, the LFMR will be enhanced due to the series of the high-resistance MTJs of L/N/L. Thus we can explain the enhanced LFMR in the composite films with the nano-columnar structure in the wide temperature range. Finally, for the films with the multi-layer structure, as shown in Figure 10c, electric current flows through the high transport channels of the LSMO layer without any MTJs tune effect. The resistance can be simply described as $1/\rho = A''(H)/\rho_{\text{LSMO}} + B''(H)/\rho_{\text{NiO}}$. In fact, because $\rho_{\text{LSMO}} \ll \rho_{\text{NiO}}$, so the LFMR is almost in line with the pure LSMO thin films. Based on the experimental and analysis results above, the LFMR properties can be tuned by modulating the microstructure of the composite films, thus it provides a viable route to manipulate the LFMR.

3. Conclusion

In this study, $\text{La}_{0.7}\text{Sr}_{0.3}\text{MnO}_3$ (LSMO):NiO nanocomposite films with different microstructures have been grown on the SrTiO_3 (001) substrate by pulsed laser deposition, and their tunable magnetic properties and low-field magnetoresistance (LFMR) from 2 K to room temperature have been investigated. The experimental results show that the LSMO:NiO nanocomposite films with NiO volume ratio of 50% have a checkerboard-like structure, while those with NiO volume ratio of 70% have a nano-columnar structure. The composite films with the checkerboard-like structure exhibit a large LFMR in the high temperature range from 200 to 300 K with the highest value of 17% at 250 K under a magnetic field of 1 T. Correspondingly, a large LFMR in the low temperature range from 10 to 210 K with the maximum value of 41% at 10 K under a magnetic field of 1 T is obtained in the composite films with the nano-columnar structure. A series parallel circuit model is proposed to understand the effect of microstructures on the LFMR value and its working temperature. Our results demonstrate that controlling the microstructures in the LSMO:NiO composite films is a key role to modulate the LFMR value in different temperature ranges.

4. Experimental Section

Single-crystal SrTiO_3 (STO) substrates with (001) orientation were cleaned in an ultrasonic bath with acetone followed by ethanol. The LSMO-NiO nanocomposite thin films were grown on the STO substrates by pulsed laser deposition (PLD) using a KrF ($\lambda = 248$ nm) excimer

laser, with a flux of approximately 1.4 J cm^{-2} and a repetition rate of 2 Hz under a process pressure of 0.5 mbar of pure O_2 at a substrate temperature of 670 °C for LSMO and NiO. LSMO:NiO ratios in the composite films were controlled by the deposition time of the LSMO and NiO. Detail fabrication method to tune the geometry structure of the nanocomposite films has been illustrated in the supplement materials. The fabricated samples were then annealed in pure O_2 under 0.5 Bar to remove oxygen vacancies. For comparison, the pure LSMO films were also grown on the STO substrates under the same growth and annealing conditions. Crystal structure and phases of the films were determined by X-ray diffraction (XRD; Rigaku, D/max-2000, $\text{Cu K}\alpha$ radiation) analysis. Microstructures were studied by a transmission electron microscopy (TEM) (F20, Tecnai). Specimens for TEM study were ground and polished to a thickness of 20 μm and were further thinned to perforation by Ar-ion milling using a Gatan precision ion polishing system (PIPS, Gatan 691, Gatan Inc.). Chemical state of the elements and NiO ratios in the composite films were determined by X-ray photoelectron spectroscopy (XPS, Thermo ESCALAB 250; Al $\text{K}\alpha$ source, 1486.60 eV, Resolution: 400 meV, Energy step: 0.1 eV). Magnetization measurements were performed from 5 to 340 K and in external magnetic fields up to 0.3 T using a superconducting quantum interference device (SQUID) magnetometer. Transport properties were measured by the standard four-terminal method in the range from 2 K to 340 K using a physical property measurement system (PPMS).

Supporting Information

Supporting Information is available from the Wiley Online Library or from the author.

Acknowledgements

The partial support of this work by the Hundred Talents Program of Chinese Academy of Sciences, the National Natural Science of foundation of China (No. 51172238) and the National Basic Research Program (No.2010CB934603) of China, Ministry of Science and Technology China is gratefully acknowledged.

Received: March 5, 2014

Revised: April 19, 2014

Published online:

- [1] Z. Bi, E. Weal, H. Luo, A. Chen, J. L. MacManus-Driscoll, Q. Jia, H. Wang, *J. Appl. Phys.* **2011**, *109*, 054302.
- [2] Y. M. Kang, H. J. Kim, S. I. Yoo, *Appl. Phys. Lett.* **2009**, *95*, 052510.
- [3] S. J. Zhu, J. Yuan, B. Y. Zhu, F. C. Zhang, B. Xu, L. X. Cao, X. G. Qiu, B. R. Zhao, P. X. Zhang, *Appl. Phys. Lett.* **2007**, *90*, 112502.
- [4] S. Ornes, *Proc. Natl. Acad. Sci. USA* **2013**, *110*, 3710.
- [5] P. K. Siwach, H. K. Singh, O. N. Srivastava, *J. Phys.: Condens. Matter.* **2008**, *20*, 273201.
- [6] B. B. Nelson-Cheeseman, F. J. Wong, R. V. Chopdekar, E. Arenholz, Y. Suzuki, *Phys. Rev. B* **2010**, *81*, 214421.
- [7] P. P. Deen, F. Yokaichiya, A. de Santis, F. Bobba, A. R. Wildes, A. M. Cucolo, *Phys. Rev. B* **2006**, *74*, 224414.
- [8] H. Y. Hwang, S.-W. Cheong, N. P. Ong, B. Batlogg, *Phys. Rev. Lett.* **1996**, *77*, 2041.
- [9] H. Li, J. R. Sun, H. K. Wong, *Appl. Phys. Lett.* **2002**, *80*, 628.
- [10] S. Jin, T. H. Tiefel, M. McCormack, R. A. Fastnacht, R. Ramesh, L. H. Chen, *Science* **1994**, *264*, 413.
- [11] V. Moshnyaga, B. Damaschke, O. Shapoval, A. Belenchuk, J. Faupel, O. I. Lebedev, J. Verbeeck, G. Van Tendeloo, M. Mücksch, V. Tsurkan, R. Tidecks, K. Samwer, *Nat. Mater.* **2003**, *2*, 247.
- [12] Z. G. Sheng, Y. P. Sun, X. B. Zhu, W. H. Song, P. Yan, *J. Phys. D: Appl. Phys.* **2007**, *40*, 3300.

- [13] D. Bhadra, M. G. Masud, S. K. De, B. K. Chaudhuri, *Appl. Phys. Lett.* **2013**, *102*, 072902.
- [14] S. A. Fedoseev, A. V. Pan, S. Rubanov, I. A. Golovchanskiy, O. V. Shcherbakova, *ACS Nano* **2013**, *7*, 286.
- [15] Z. F. Zi, Y. Fu, Q. Liu, J. Dai, Y. Sun, *J. Magn. Magn. Mater.* **2012**, *324*, 1117.
- [16] D. T. Tran, T. H. Nguyen, H. M. Do, D. L. Vu, T.-L. Phan, S.-C. Yu, *Adv. Nat. Sci.: Nanosci. Nanotechnol.* **2013**, *4*, 035001.
- [17] M. Staruch, D. Hires, A. Chen, Z. Bi, H. Wang, M. Jain, *J. Appl. Phys.* **2011**, *110*, 113913.
- [18] S. Valencia, O. Castaño, J. Fontcuberta, B. Martínez, Ll. Balcells, *J. Appl. Phys.* **2003**, *94*, 2524.
- [19] Y. K. Tang, X. F. Ge, X. F. Si, W. J. Zhao, Y. Wang, S. Dong, Y. Zhai, Y. Sui, W. H. Su, C. C. Almasan, *Phys. Status Solidi A* **2013**, *210*, 1195.
- [20] Z. L. Liao, P. Gao, S. Stadler, R. Y. Jin, X. Q. Pan, E. W. Plummer, J. D. Zhang, *Appl. Phys. Lett.* **2013**, *103*, 043112.
- [21] A. Chen, Z. Bi, C.-F. Tsai, J. Lee, Q. Su, X. Zhang, Q. Jia, J. L. MacManus-Driscoll, H. Wang, *Adv. Funct. Mater.* **2011**, *21*, 2423.
- [22] L. Li, X. Q. Zhang, L. Li, X. F. Zhai, C. G. Zeng, *Solid State Commun.* **2013**, *171*, 46.
- [23] J. Li, Q. Huang, Z. W. Li, L. P. You, S. Y. Xu, C. K. Ong, *J. Appl. Phys.* **2001**, *89*, 7428.
- [24] X. W. Li, A. Gupta, G. Xiao, G. Q. Gong, *Appl. Phys. Lett.* **1997**, *71*, 1124.
- [25] R. N. Mahato, H. Lülff, M. H. Siekman, S. P. Kersten, P. A. Bobbert, M. P. de Jong, L. De Cola, W. G. van der Wiel, *Science* **2013**, *341*, 257.
- [26] P. Dey, T. K. Nath, *Phys. Rev. B* **2006**, *73*, 214425.
- [27] A. Sadhu, S. Bhattacharyya, *Chem. Mater.* **2014**, *26*, 1702.
- [28] T. H. Kim, M. Uehara, S.-W. Cheong, S. Lee, *Appl. Phys. Lett.* **1999**, *74*, 1737.
- [29] H. J. Liu, V. T. Tra, Y. J. Chen, R. Huang, C. G. Duan, Y. H. Hsieh, H. J. Lin, J. Y. Lin, C. T. Chen, Y. C. Ikuhara, Y. H. Chu, *Adv. Mater.* **2013**, *25*, 4753.
- [30] J. L. MacManus-Driscoll, P. Zerrer, H. Wang, H. Yang, J. Yoon, S. R. Foltyn, M. G. Blmire, Q. X. Jia, *Nat. Mater.* **2008**, *7*, 314.
- [31] M. Staruch, H. Gao, P.-X. Gao, M. Jain, *Adv. Funct. Mater.* **2012**, *22*, 3591.
- [32] W. R. Zhang, A. P. Chen, F. Khatkatay, C.-F. Tsai, Q. Su, L. Jiao, X. H. Zhang, H. Y. Wang, *ACS Appl. Mater. Interface* **2013**, *5*, 3995.
- [33] A. P. Chen, W. R. Zhang, J. Jian, H. Y. Wang, C.-F. Tsai, Q. Su, Q. X. Jia, J. L. MacManus-Driscoll, *J. Mater. Res.* **2013**, *28*, 1707.
- [34] B. S. Kang, H. Wang, J. L. MacManus-Driscoll, Y. Li, Q. X. Jia, *Appl. Phys. Lett.* **2006**, *88*, 192514.
- [35] S. Kang, A. Goyal, J. Li, A. A. Gapud, P. M. Martin, L. Heatherly, J. R. Thompson, D. K. Christen, F. A. List, M. Paranthanman, D. F. Lee, *Science* **2006**, *311*, 1911.
- [36] J. L. MacManus-Driscoll, *Adv. Funct. Mater.* **2010**, *20*, 2035.
- [37] T. Obata, T. Manako, Y. Shimakawa, Y. Kubo, *Appl. Phys. Lett.* **1999**, *74*, 290.
- [38] X. F. Liu, J. Shi, *Appl. Phys. Lett.* **2013**, *102*, 202401.
- [39] B. X. Huang, Y. H. Liu, R. Z. Zhang, X. B. Yuan, C. J. Wang, L. M. Mei, *J. Phys. D: Appl. Phys.* **2003**, *36*, 1923.
- [40] K. Tanaka, S. Okamura, T. Shiosaki, *Jpn. J. Appl. Phys.* **2001**, *40*, 6821.
- [41] X. K. Ning, Z. J. Wang, X. G. Zhao, C. W. Shih, Z. D. Zhang, *J. Appl. Phys.* **2013**, *113*, 223903.
- [42] B. S. Guiton, P. K. Davies, *Nat. Mater.* **2007**, *6*, 586.
- [43] A. P. Chen, W. R. Zhang, F. Khatkatay, Q. Su, C. F. Tsai, L. Chen, Q. X. Jia, J. L. MacManus-Driscoll, H. Wang, *Appl. Phys. Lett.* **2013**, *102*, 093114.
- [44] F. J. Wong, S. B. Zhu, J. M. Iwata-Harms, Y. Suzuki, *J. Appl. Phys.* **2012**, *111*, 063920.
- [45] P. T. Phong, N. V. Khiem, N. V. Dai, D. H. Manh, L. V. Hong, N. X. Phuc, *Mater. Lett.* **2009**, *63*, 353.
- [46] S. L. Yuan, Y. P. Yang, Z. C. Xin, G. Peng, G. H. Zhang, J. Tang, J. Liu, L. J. Zhang, Q. H. Zhong, S. Liu, L. Chen, W. Feng, Z. Y. Li, L. Liu, G. Q. Zhang, F. Tu, C. S. Xiong, *Solid State Commun.* **2002**, *123*, 55.
- [47] D. B. Williams, C. B. Carter, *Transmission Electron Microscopy: A Textbook for Materials Science*, Plenum, New York **1996**.
- [48] B. S. Guiton, H. Wu, P. K. Davies, *Chem. Mater.* **2008**, *20*, 2860.
- [49] Y. Ni, W. F. Rao, A. G. Khachatryan, *Nano Lett.* **2009**, *9*, 3275.
- [50] X. Liang, D. R. Clarke, *Acta Mater.* **2014**, *63*, 191.
- [51] C. Wang, N. Stojic, N. Binggeli, *Appl. Phys. Lett.* **2013**, *102*, 152414.
- [52] E. T. Wertz, Q. Li, *Appl. Phys. Lett.* **2007**, *90*, 142506.
- [53] Y. P. Lee, S. Y. Park, Y. H. Hyun, J. B. Kim, V. G. Prokhorov, V. A. Komashko, V. L. Svetchnikov, *Phys. Rev. B* **2006**, *73*, 224413.
- [54] M. Eshraghi, H. Salamati, P. Kameli, *J. Alloys Compd.* **2007**, *437*, 22.
- [55] M. Eshraghi, H. Salamati, P. Kameli, *J. Phys.: Condens. Matter.* **2006**, *18*, 8281.
- [56] S. M. Wu, S. A. Cybart, P. Yu, M. D. Rossell, J. X. Zhang, R. Ramesh, R. C. Dynes, *Nat. Mater.* **2010**, *9*, 756.
- [57] E. Choi, E. Weal, Z. Bi, H. Y. Wang, A. Kursumovic, T. Fix, M. G. Blamire, J. L. MacManus-Driscoll, *Appl. Phys. Lett.* **2013**, *102*, 012905.
- [58] Y. Q. Guo, L. Shi, S. M. Zhou, J. Y. Zhao, W. J. Liu, *Appl. Phys. Lett.* **2013**, *102*, 222401.
- [59] J. M. De Teresa, M. R. Ibarra, J. Blasco, J. García, C. Marquina, P. A. Algarabel, Z. Arnold, K. Kamenev, C. Ritter, R. Von Helmolt, *Phys. Rev. B* **1996**, *54*, 1187.
- [60] C. H. Yan, Z. G. Xu, T. Zhu, Z. M. Wang, F. X. Cheng, Y. H. Huang, C. S. Liao, *J. Appl. Phys.* **2000**, *87*, 5588.
- [61] M. Staruch, C. Cantoni, M. Jain, *Appl. Phys. Lett.* **2013**, *102*, 062416.
- [62] P. Sheng, B. Abeles, *Phys. Rev. Lett.* **1972**, *28*, 34.
- [63] A. Bhatnagar, A. Roy Chaudhuri, Y. H. Kim, D. Hesse, M. Alexe, *Nat. Commun.* **2013**, *4*, 2835.